

In Situ Formation of Nano Ni–Co Oxyhydroxide Enables Water Oxidation Electrocatalysts Durable at High Current Densities

Jehad Abed, Shideh Ahmadi, Laura Laverdure, Ahmed Abdellah, Colin P. O'Brien, Kevin Cole, Pedro Sobrinho, David Sinton, Drew Higgins, Nicholas J. Mosey, Steven J. Thorpe,* and Edward H. Sargent*

The oxygen evolution reaction (OER) limits the energy efficiency of electrocatalytic systems due to the high overpotential symptomatic of poor reaction kinetics; this problem worsens over time if the performance of the OER electrocatalyst diminishes during operation. Here, a novel synthesis of nanocrystalline Ni–Co–Se using ball milling at cryogenic temperature is reported. It is discovered that, by anodizing the Ni–Co–Se structure during OER, Se ions leach out of the original structure, allowing water molecules to hydrate Ni and Co defective sites, and the nanoparticles to evolve into an active Ni–Co oxyhydroxide. This transformation is observed using operando X-ray absorption spectroscopy, with the findings confirmed using density functional theory calculations. The resulting electrocatalyst exhibits an overpotential of 279 mV at 0.5 A cm⁻² and 329 mV at 1 A cm⁻² and sustained performance for 500 h. This is achieved using low mass loadings (0.36 mg cm⁻²) of cobalt. Incorporating the electrocatalyst in an anion exchange membrane water electrolyzer yields a current density of 1 A cm⁻² at 1.75 V for 95 h without decay in performance. When the electrocatalyst is integrated into a CO₂-to-ethylene electrolyzer, a record-setting full cell voltage of 3 V at current density 1 A cm⁻² is achieved.

fuel and chemical feedstocks, mitigating the variability challenge of renewable energy.^[1–3] However, the efficiency of these electrocatalytic systems is limited by the sluggish kinetics and high overpotentials at the anode imposed by the oxygen evolution reaction (OER).^[4] A relatively small selection of OER electrocatalysts meets the requirements needed for industrial electrocatalysis: low OER overpotentials (<300 mV) at high current densities (>500 mA cm⁻²) for long-term operation (ultimately >60 000 h).^[5] Identifying durable and efficient OER electrocatalysts is urgently needed to enable large-scale industrial implementation of important electrocatalytic technologies such as water splitting and CO₂R.

To date, benchmark noble electrocatalysts based on RuO_x and IrO_x are considered state-of-the-art OER electrocatalysts in view of their superior performance; unfortunately, their high price and scarcity limit their widespread application.


In contrast, earth abundant metal oxides, selenides, nitrides, and phosphides derived from the first-row transition metals Ni, Co, and Fe can offer a cheaper alternative for efficient OER electrocatalysts in anion exchange membrane (AEM) systems, which use an alkaline environment that is more compatible with non-noble-metal electrocatalysts than an acidic environment.

1. Introduction

With the large anticipated penetration of low-cost renewable electricity into the power grid comes the need for cost-effective decarbonization strategies combined with large-scale storage. Water splitting and CO₂ reduction (CO₂R) can store electricity in the form of stable chemical bonds in synthetic

J. Abed, K. Cole, P. Sobrinho, S. J. Thorpe
Department of Materials Science and Engineering
University of Toronto
184 College Street, Toronto, Ontario M5S 3E4, Canada
E-mail: steven.thorpe@utoronto.ca

J. Abed, E. H. Sargent
Department of Electrical and Computer Engineering
University of Toronto
35 St George Street, Toronto, Ontario M5S 1A4, Canada
E-mail: ted.sargent@utoronto.ca

 The ORCID identification number(s) for the author(s) of this article can be found under <https://doi.org/10.1002/adma.202103812>.

S. Ahmadi, L. Laverdure, N. J. Mosey
Department of Chemistry
Queen's University
90 Bader Lane, Kingston, Ontario K7L 3N6, Canada

A. Abdellah, D. Higgins
Department of Chemical Engineering
McMaster University
Hamilton, Ontario L8S 4L7, Canada

C. P. O'Brien, D. Sinton
Department of Mechanical and Industrial Engineering
University of Toronto
5 King's College Road, Toronto, Ontario M5S 3G8, Canada

DOI: 10.1002/adma.202103812

One of the most efficient non-noble OER electrocatalysts in alkaline systems is Fe-doped NiOOH.^[6–8] While a small amount of Fe can boost the OER electrocatalytic activity of NiOOH, it has been reported that Fe segregates from the Ni–Fe oxyhydroxide lattice to form a secondary FeOOH phase that deactivates the electrocatalyst.^[9] Berlinguette and co-workers found that at 200 mA cm⁻² in strong base electrolytes, NiFeO_x OER electrocatalyst had a similar degradation problem as a significant amount of Fe left the structure and diffused to the cathode.^[10] Furthermore, Markovic and co-workers investigated the activity and stability trends for monometallic oxyhydroxides and observed that Fe is the least stable compared to Ni and Co.^[11] These findings motivate the development of an Fe-free earth abundant OER electrocatalyst that is both active and stable in alkaline conditions.

Among candidates to replace Fe in Ni electrocatalysts, Co is known to lower the OER overpotential and improve electrochemical stability.^[12,13] However, as Co is heavily used in energy applications, especially Li-ion batteries, it is anticipated that it may suffer from supply shortages in future.^[14] This mandates the development of methods to reduce Co loadings in energy materials. Here we deploy Se, a chalcogenide, with Ni and Co, to serve as a sacrificial scaffold to enable the efficient activation of small mass loadings of Co in the electrocatalyst during OER. Prior reports have shown that metal selenides are thermodynamically unstable during OER at high pH, resulting in structural changes such as increased nanoporosity, disordering in the lattice, and high density of defective surface sites.^[15–17] We lever these localized structural changes to form, in situ amorphous nano Ni–Co oxyhydroxides with high mass and specific activities.

Synthesizing metal chalcogenides has previously proven challenging due to the immiscibility of the constituent elements and the need for high thermal activation temperatures >500 °C.^[18] We used cryomilling—ball milling at cryogenic temperatures—to synthesize well-mixed Ni–Co–Se electrocatalysts. Milling at such low temperatures provided us with control over a wide compositional range of the compound and enabled the formation of amorphous structures. Amorphous metals have been produced by a variety of methods: atomization, electrodeposition, electroless deposition, planar and flow casting. However, amorphous alloys produced by these methods are limited to a narrow compositional range near low melting point eutectics, unlike cryomilling which can produce a wider range of amorphous phases centered around high melting point intermetallics. Accordingly, targeting Ni–Co–Se compositions with a high melting point favors disordering and the formation of abundant defective and coordinatively unsaturated sites (CUS) that can facilitate the hydration of Ni and Co sites and the formation of oxyhydroxides.^[12,16,19–22] After synthesis, we activated Ni–Co–Se by subjecting it to OER conditions and evaluating its half-cell activity and stability at high current densities >100 mA cm⁻². The activation process was investigated using operando X-ray absorption spectroscopy (XAS), electron energy-loss spectroscopy (EELS), and density functional theory (DFT) calculations. We find that Se leaches, induces surface reconstruction during OER, and facilitates the hydration of metal centers to form active oxyhydroxides. We study the performance of Ni–Co–Se as OER electrocatalyst with respect to requirements for

water splitting and CO₂R in a 5 cm² AEM-based membrane-electrode-assembly (MEA) electrolyzer. We report a full cell voltage delivering 1 A cm⁻² at 1.75 V for water splitting and 3 V for CO₂R.

2. Results and Discussion

2.1. Synthesis and Activation of Electrocatalysts

The electrocatalysts were synthesized using a one-pot ball milling process in two steps: mechanical alloying at a cryogenic temperature (<–196 °C) to produce disordered structures and surfactant-assisted ball milling (SABM) at room temperature to reduce the size of the alloy to nanoparticles (Figure 1a). The combination of high-speed mixing (30 Hz, 1800 rpm) and low temperature (–196 °C) facilitates the formation of nanocrystalline structures centered at high-melting point compositions (see the Supporting Information for synthesis description).

First, Ni–Se and Co–Se control samples were synthesized to investigate the milling behavior of Ni and Co with Se and to confirm the formation of metal selenide phases without the need for thermal activation. We observed characteristic X-ray diffraction (XRD) peaks of binary metal selenide phases after just 6 h of cryomilling and no peaks for elemental Ni, Co, or Se, indicative of full incorporation of Se in a mixed Ni–Co selenide structure (Figures S1 and S2, Supporting Information). Due to the high kinetic energy induced by ball–powder–ball collisions at high speeds, alloying is facilitated by repeated fracture and cold welding of the particles, while crystal defects and the local rise in temperature aids the diffusion of elements in the alloyed structure.^[23] We found that, despite the possibility of particles welding together due to excessive collisions during milling, Se played an important role in stabilizing single phase nanoparticles (<100 nm) with Ni and Co (see the Supporting Information). To reduce Fe contamination from the stainless steel balls and the walls of the vial during milling, we run the mill for a few minutes with the starting precursors to cover all the inside walls of the vial and the surface of the balls with a thick layer of the precursor and prevent direct collision with any Fe. Using inductively coupled plasma atomic emission spectroscopy (ICP-AES), we found that the Fe concentration in the catalyst after cryomilling was limited to 0.05 ± 0.03 at% (see the Supporting Information for experimental details).

Afterward, we synthesized Ni–Co–Se compounds centered about two high-melting point compositions: (NiCo)Se and (NiCo)₃Se₄. The particles of Ni–Co–Se compounds had an average size greater than 1 μm and a small surface-to-volume ratio, which is undesirable for electrocatalysis. Therefore, a surfactant was used in the second SABM step to reduce the particle size of the alloyed compounds to 67 nm for (NiCo)₃Se₄ and 37 nm for (NiCo)Se (Figure 1c; Figures S4–S6, Supporting Information). The broad diffraction peaks in XRD indicated that nanosized crystallites (8.37 nm) were produced after SABM (Figure 1b, see the Supporting Information for calculations). Finally, the surfactant was removed from the surface of the alloy after synthesis via washing. After milling, the particles were sonicated for 30 min in ethanol before centrifuging at 10000 rpm (11000 rcf) for 1 h, and then the clear solution

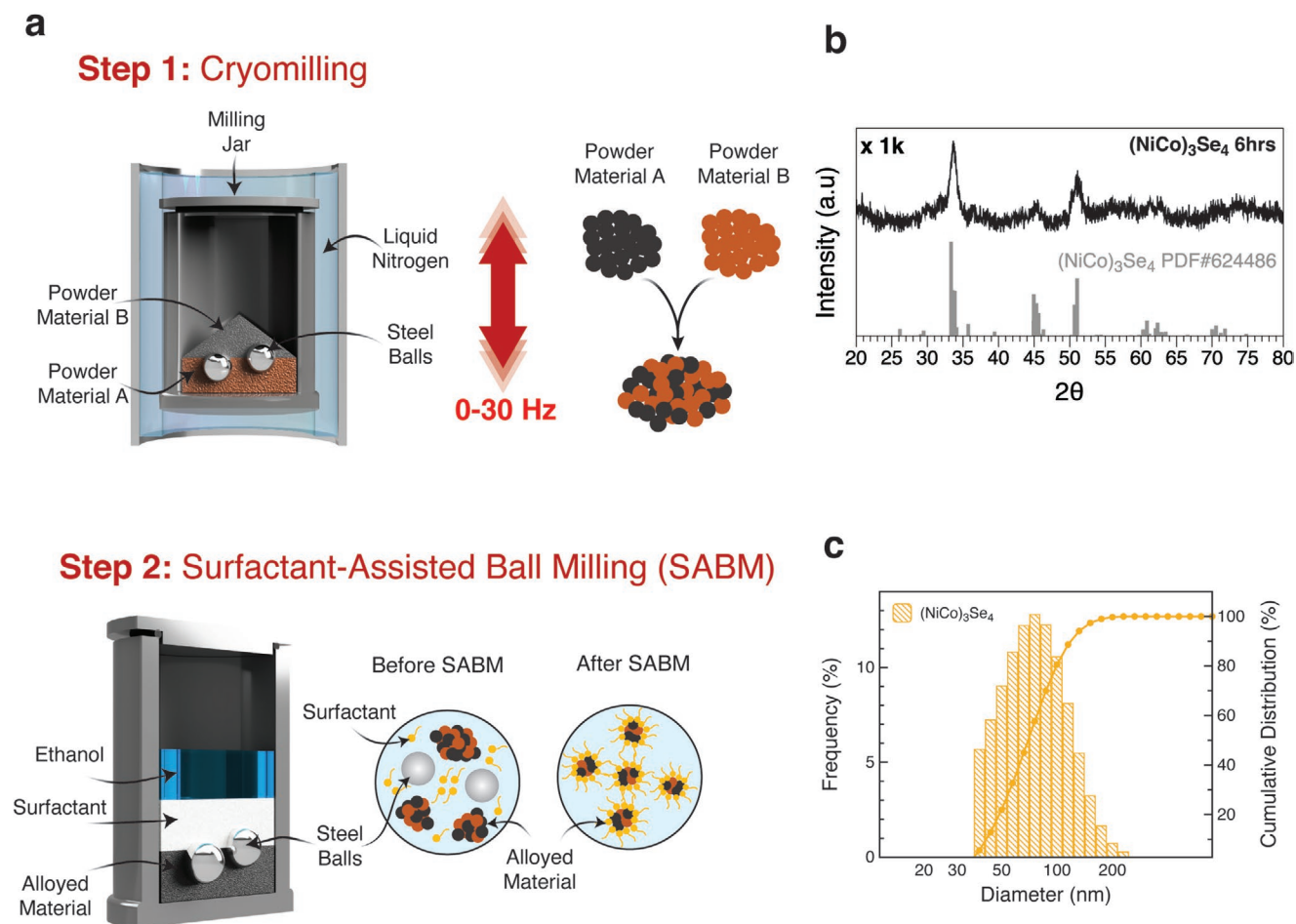


Figure 1. Schematic illustration of the two-step synthesis process: a) Step 1: milling at a cryogenic temperature $-196\text{ }^{\circ}\text{C}$ to alloy elements, Step 2: milling in wet environment using surfactant to reduce the size of the alloyed particles. b) XRD of $(\text{NiCo})\text{Se}$ and $(\text{NiCo})_3\text{Se}_4$ after 6 h of cryomilling and 10 h of SABM. c) Particle size distribution for $(\text{NiCo})\text{Se}$ and $(\text{NiCo})_3\text{Se}_4$ after SABM for 10 h followed by centrifuging at 6000 rpm for 1 h.

was washed and replaced with fresh ethanol: this procedure was repeated three times until the nanoparticles precipitated to the bottom of the tube. Thermogravimetric analysis (TGA) was conducted to evaluate the extent of removal of the surfactant species after washing. The uncleaned sample had $\approx 2\text{ wt}\%$ mass loss attributed to the residual surfactant, whereas there was a negligible mass loss ($<0.001\text{ wt}\%$, below the detection limit of the instrument) for the washed particles, indicating the washing step was effective in removing the surfactant (Figure S7, Supporting Information). In summary, Se played an important role in tailoring the size and crystal structure of the cryomilled alloys. Cryomilling Ni–Co without Se produces large ($>6\text{ }\mu\text{m}$) crystalline particles which are not amorphized even under prolonged milling times (Figure S3, Supporting Information).

We then activated $(\text{NiCo})\text{Se}$ and $(\text{NiCo})_3\text{Se}_4$ electrochemically by selectively leaching Se out of the nanocrystalline structure (Figure 2a). According to the Pourbaix diagram of Se, Se oxidizes to soluble $\text{SeO}_3^{2-}/\text{SeO}_4^{2-}$ at high pH during the OER. The activation process was conducted in 1 M of pre-electrolyzed KOH, to purify the electrolyte from Fe ions that could participate in the reaction (Figure S8, Supporting Information), and initiated by applying a constant current density of

$10\text{ mA cm}_{\text{geo}}^{-2}$ in a three-electrode cell for 2 h, a sufficient time to warrant a complete removal of Se.^[15]

Scanning electron microscopy (SEM) images were taken for the as-synthesized $(\text{NiCo})_3\text{Se}_4$ samples before and after activation (Figure 2b). Clusters of nanoparticles were observed in the as-synthesized sample and Se accounted for 56 at% in the structure. After activation, the morphology of the clusters was altered and Se was completely removed (0 at%, as confirmed by energy dispersive spectroscopy [EDS]), while the atomic ratio between Ni and Co remained unchanged (1:1). TEM and electron energy loss spectroscopy (EELS) mapping were conducted on the as-synthesized (Figure 2c) and activated samples (Figure 2d). EELS elemental maps showed that Ni, Co, and Se in the as-synthesized $(\text{NiCo})_3\text{Se}_4$ were homogeneously distributed in $\approx 10\text{ nm}$ nanoparticles. This was also seen by scanning transmission electron microscopy (STEM) and EDS (Figure S6, Supporting Information). EELS spectra were acquired from the areas indicated in the elemental maps (Figure S9, Supporting Information). Using EELS $L_{2,3}$ edge position, the oxidation state of Ni and Co in the as-synthesized sample was determined to be 2+ (Figure S10a,b, Supporting Information), this, in addition to the lack of O signal inside the particles as shown by the O EELS

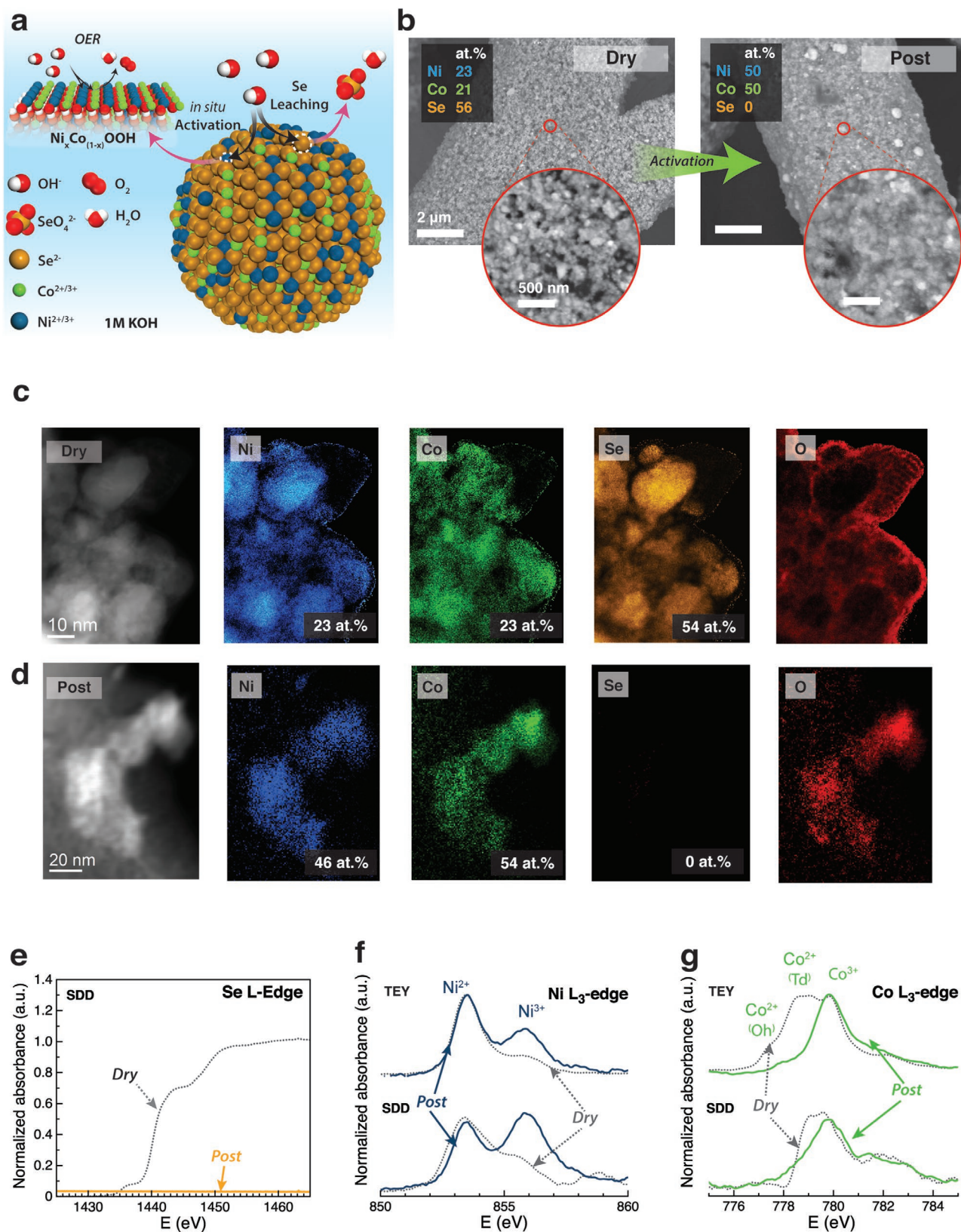


Figure 2. a) A schematic of the activation process for Ni–Co–Se alloys. b) BSE-SEM images and c,d) TEM images of the $(\text{NiCo})_3\text{Se}_4$ catalyst at 0 h (dry) and after 2 h of activation at 10 mA cm^{-2} (post). The elemental content of the catalyst is shown in the inset tables. e,f) Soft X-ray L-edge XANES of Se using SDD (e) and Ni (f) and Co (g) using TEY and SDD.

map (Figure 2d and Figure S9a, Supporting Information), confirmed that Ni and Co were incorporated in the selenide structure forming Ni–Co–Se. After activation, Se was not detected in the catalyst structure using EELS (Figure 2c and Figure S10c, Supporting Information), confirming that Se was completely leached out of the structure during electrochemical activation while O was present throughout the particles. The EELS $L_{2,3}$ edge position of Ni and Co showed that the oxidation state of both Ni and Co were increased to 3+ after activation (Figure S10a,b, Supporting Information). Furthermore, we conducted ICP-AES on the catalyst during the first 48 h of the OER (Figure S11, Supporting Information). We observed that Se dissolved within the first ≈ 10 min of the OER confirming EELS and EDS observations. On the other hand, both Ni and Co remained intact in the catalyst as the total ions dissolved amounts were below the background equivalent concentrations (BEC) for Ni (17 ppb) and Co (12 ppb), respectively. XRD and electron diffraction pattern (DP) using TEM were collected after the activation of the sample to investigate the changes in the crystal structure of the catalyst. Both techniques confirmed the change in crystal structure during activation as indicated by the amorphous rings in DP and the lack of diffraction peaks in XRD (Figures S12 and S13, Supporting Information). Diffraction rings at 2.5, 2.1, 1.5 Å were clearly observed, corresponding to the (111), (100), and (110) crystal planes of CoO/Co(OH)₂, carbon, and Ni(OH)₂, respectively.^[24,25]

To characterize the materials further, soft X-ray absorption spectroscopy (sXAS) was conducted to investigate the local chemical and electronic changes to individual Ni, Co, and Se atoms after activation. Using a silicon drift detector (SDD), the X-ray absorption near edge structure (XANES) of Se L-edge was obtained. This revealed that Se was incorporated in the dry nanoparticles as selenide (Se²⁻) and that it departed the structure after activation as indicated by the lack of the Se L-edge signal after 2 h of OER (Figure 2e).^[26] The oxidation states of Ni and Co were inspected after activation as shown in XANES of L₃-edge results (Figure 2f,g). Two different modes of X-ray detection were used to investigate the oxidation state: fluorescence X-rays using SDD and total electron yield (TEY). The TEY mode is dependent on the conductivity of the surface but is more surface sensitive (<10 nm) compared to SDD (within 100 nm). Using both detection modes allowed us to investigate the changes in oxidation state within the bulk and on the surface of the electrocatalysts before and after activation. The XANES of Ni L₃-edge of the dry sample revealed that Ni had an oxidation state of 2+ before activation while Co in the as-synthesized sample had a mixed oxidation state of 2+/3+ on the surface implying that Co was in a spinel structure.^[27] The oxidation state of Ni and Co increased to 3+ after activation possibly suggesting the transformation to NiCoOOH.^[28,29] Therefore, we will start describing the catalysts after activation in the following sections as “activated” to reflect the nature of the final structure which is NiCoOOH.

2.2. Electrocatalytic Performance and Stability

The performance of catalysts after activation was evaluated by measuring the overpotential at 10 mA cm_{geo}⁻² on a glassy

carbon electrode as in (Figure 3a). The activity of activated (NiCo)Se and (NiCo)₃Se₄ after SABM (NiCoOOH) improved dramatically due to an increase in the surface-to-volume ratio of the nanoparticles. Alloying Ni and Co in the electrocatalyst lowered the overpotential compared to binary NiSe and CoSe alone by ≈ 50 mV confirming that Ni and Co have synergistic effects when alloyed together.^[12,30] The best performance was seen for activated (NiCo)₃Se₄ (NiCoOOH) after SABM with an overpotential of 268 ± 2 mV at 10 mA cm_{geo}⁻² and a Tafel slope of 42 mV dec⁻¹ (Figures S14 and S15, Table S4, Supporting Information).

To examine the specific catalytic activity, we normalized the current density by the electrochemical surface area (ECSA) using double-layer capacitance measured by cyclic voltammetry (CV) (Figures S16 and S17, Supporting Information). Activated (NiCo)₃Se₄ (NiCoOOH) demonstrated ECSA current densities four times higher than commercial IrO₂ using the same catalyst loading of 0.21 mg cm⁻² for all electrocatalysts (Figure 3b). The turnover frequency (TOF) of the catalyst was calculated as 50.76×10^{-3} s⁻¹ per site, considering only Ni and Co as active sites, approximately twofolds higher than IrO₂ 28.09×10^{-3} per site implying activated (NiCo)₃Se₄ (NiCoOOH) is intrinsically more active.

We then investigated the stability of the catalyst using chronopotentiometry at 10 mA cm_{geo}⁻² (Figure S18, Supporting Information). The catalyst maintained a steady overpotential value of 267 mV for 100 h with only 4 mV overpotential increase. At higher current densities and prolonged testing conditions, excessive oxygen bubbling can artificially increase the overpotential by shielding the active sites on the surface and within the pores of the electrocatalyst. Rotating disk electrodes (RDEs) are often used to overcome this problem and improve the detachment of bubbles from the surface of the electrocatalyst and lower mass transport limitations by rotation. However, vigorous rotation for long duration has been reported to affect the binding of the electrocatalyst to the surface of the RDE implying fallacious conclusions about the intrinsic stability of the electrocatalyst.^[31] Therefore, we proposed an alternating current test (ACT) to better assess the intrinsic stability of the electrocatalyst by removing bubbles without mechanical rotation. In ACT, a constant current density of 10 mA cm_{geo}⁻² was applied to the catalyst for 10 h, and then it was allowed to rest at open-circuit potential (OCP) for 1 h to release O₂ bubbles on the surface before evaluating the performance using linear sweep voltammetry (LSV); this resembles one cycle of testing (Figure 3c). The potential slowly increased during the first few hours of each cycle because of bubble accumulation on the surface; however, the initial potential was retained in the following cycle suggesting that bubbles were partially or completely released. The test was repeated for 34 cycles (340 h of operation). After each cycle, the overpotential and Tafel slope were extracted and plotted with respect to time (Figure 3d). The electrocatalyst experienced a marginal increase in overpotential (<10 mV) during the entire test while the Tafel slope remained unchanged suggesting that the reaction mechanism was not altered.

The performance of catalyst on nickel foam (NF) was tested at high current densities, the overpotential was 279 mV at 0.5 A cm_{geo}⁻² and 329 mV at 1 A cm_{geo}⁻² (Figure S19,

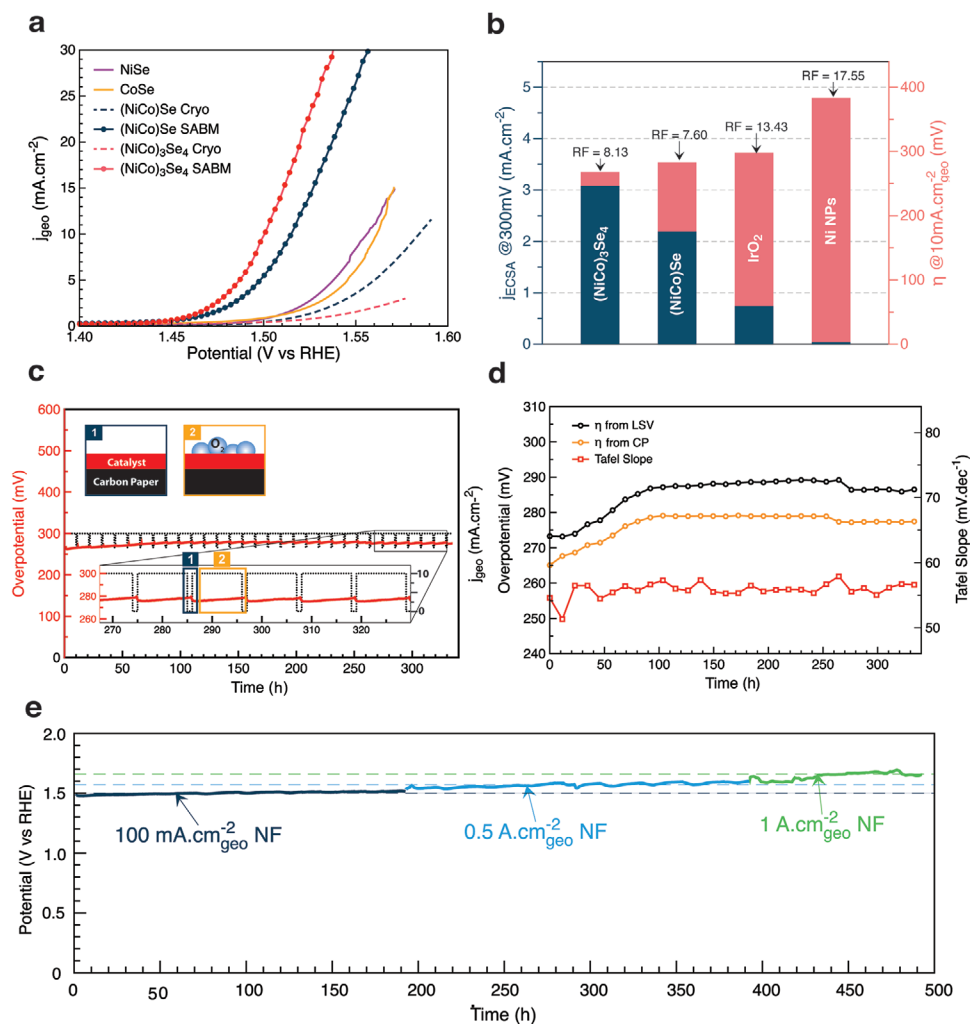


Figure 3. a) iR-corrected polarization curves on glassy carbon electrode with a loading of 0.21 mg cm^{-2} . b) Specific activity of activated $(\text{NiCo})_3\text{Se}_4$ and $(\text{NiCo})\text{Se}$ compared to IrO_2 , normalized by ECSA at 300 mV overpotential (left axis) and normalized by geometric area (right axis). The roughness factor (RF) value for each catalyst is noted at the top of the bar. c) Activated $(\text{NiCo})_3\text{Se}_4$ NP was deposited on carbon paper and tested using alternating stability test. Inset is a schematic illustration of O_2 bubble accumulation on the surface of the electrocatalyst during oxidation. d) The change in key electrochemical parameters every 10 h during the alternating stability test. e) Activated $(\text{NiCo})_3\text{Se}_4$ was deposited on Nickel foam and tested for long-term stability at high current densities. All tests were conducted in 1 M Fe-free KOH electrolyte.

Supporting Information). Next, the stability of the electrocatalyst was evaluated under constant current density (Figure 3e). The electrocatalyst had an average potential increase of 0.17 mV h^{-1} in 500 h. We compared the performance of activated $(\text{NiCo})_3\text{Se}_4$ (NiCoOOH) with the electrocatalysts from the literature which had demonstrated a durable performance at high current densities $>100 \text{ mA cm}_{\text{geo}}^{-2}$ (Table S5, Supporting Information). Our catalyst had the highest mass activities, $1395 \text{ A g}_{\text{metal}}^{-1}$, at 1 A cm^{-2} .

2.3. Electronic Structure

To investigate the active species during OER and study the dynamics of the electrochemical activation of $(\text{NiCo})_3\text{Se}_4$, in situ XAS on the K-edge of Ni, Co and Se were conducted on the sample at four conditions: dry, OCP, at 1.1 V versus RHE,

and during OER at 1.5V versus RHE (Figure 4). XANES showed that Se, in the dry sample, was present as a selenide (Se^{2-}) (Figure 4a) while Ni had an oxidation state of 2+ and Co had a mixed oxidation state of 2+/3+ suggesting that it exists in a spinel structure (Figure 4b,c), confirming EELS and sXAS findings.^[32–34] During OER, Se was oxidized to Se (VI) at 1.5 V as evident by the positive energy shift of the peak at 12666 eV while the edge position of Ni and Co continuously increased to higher energy values indicating an increase in oxidation state to 3+ during OER.^[35] Extended X-ray absorption fine structure (EXAFS) was conducted to investigate the local structure changes in the vicinity of Ni, Co, and Se atomic sites during OER (Figure 4d–f). A progressive increase in the Se-O peak at 1.7 Å after OCP was observed confirming that Se was leaching out electrochemically as SeO_4^{2-} . In the case of Ni and Co, the as-synthesized sample showed a broad peak centered around ≈ 2.3 and 2.5 Å for Ni and Co, respectively, which corresponds to

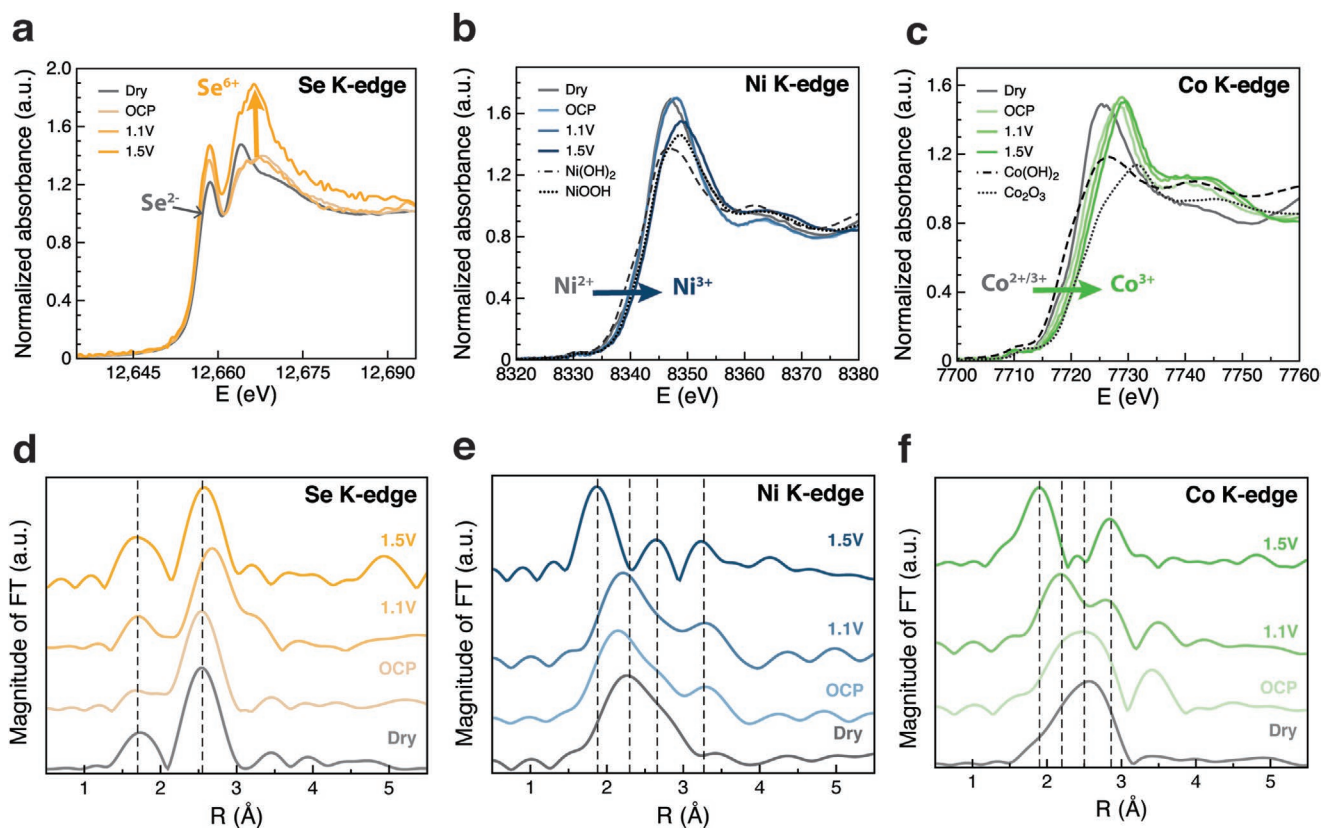


Figure 4. a–c) In situ XANES K-edge of Se (a), Ni (b), and Co (c) of $(\text{NiCo})_3\text{Se}_4$ during OER. d–f) In situ EXAFS radial distribution function of Se (d), Ni (e), and Co (f) of $(\text{NiCo})_3\text{Se}_4$ during OER. Interatomic distances noted in the figures are phase corrected using 0.5 Å shift. All tests were done in 1 M KOH.

the single scattering path Ni–Se and Co–Se confirming the local formation of Ni–Co–Se. A FEFF EXAFS fitting was performed to determine the coordination of Ni and Co after cryomilling (Figure S20, Supporting Information). The coordination of Ni was 3.5 and Co was 3.77 (Table S6, Supporting Information). Both values are lower than the coordination number of non-defective atoms in tetrahedral and octahedral sites in a Co_2NiSe_4 crystal confirming that the sites are coordinatively unsaturated after synthesis. Once the sample was placed in the electrolyte, a shoulder peak started to emerge at ≈ 2.0 Å and a new peak at ≈ 3.0 Å due to the oxidation of Ni and Co and back-scattering of Ni–O/Co–O and Ni–Ni/Co–Co in the oxyhydroxides. In the case of Co, there is an additional peak at ≈ 3.5 Å, a finding we assign to Co occupying an octahedral site in the starting spinel structure.^[36] The Ni–O peak was shifted to the left to 1.88 Å during OER (at 1.5 V) suggesting that Ni oxidized to $\gamma\text{-NiOOH}$.^[37] The Co–O peak at 1.93 Å after the OER confirms the formation of $\gamma\text{-CoOOH}$.^[38] These in situ observations agree with findings from ex situ EELS and sXAS analysis. Finally, XANES spectra were collected for the electrocatalyst after 400 h of the OER. We found that Ni oxidation state reverted to 2+ after the reaction while Co oxidation maintained a 3+ oxidation state similar to during the OER (Figure S21, Supporting Information). This indicated that, in contrast with the case of Ni, Co oxidation from 2+ to 3+ is irreversible and that the electrocatalyst is stable after 400 h of operation.

DFT calculations were used to help in explicating the experimental observations of Se leaching and of surface restructuring to an active oxide layer. Here, OER intermediates were calculated on the Ni–Se, Ni– Se_{vac} , Ni–Co–Se, and Ni–Co– Se_{vac} (001) and (101) surfaces (Figures S22–S24, Supporting Information). A Se_{vac} (Se vacancy) was used in the model to computationally study the electronic effect of the vacancies that are left behind in the structure due to Se removal by electrochemical activation, on neighboring Ni and Co atoms.

Similar results were found for both Miller indices; this discussion shall therefore focus on (101) surfaces and the details of the (001) surface can be found in the Supporting Information. The formation of adsorbed OOH on Ni–Se and Ni–Co–Se was the least enthalpically favored reaction step; so, we focus on the structural and electronic aspects for the adsorbed O and OOH. Both Ni–Se and Ni–Co–Se (101) surfaces showed a short interatomic distance of ≈ 1.7 Å between a surface Se and the adsorbed O atom (Table S7, Supporting Information). The Bader charge analysis shows the Se atom adopted a positive charge as it transferred an electron to the adsorbed O atom (Figure S25, Supporting Information). The changes to the Se atom's electronic structure closest to the adsorbed O atom on both Ni–Se and Ni–Co–Se (101) surfaces are also confirmed through their projected density of states (Figure S26, Supporting Information). The Se–O bond formed suggests the possibility of Se leaching as SeO desorption rather than continuing the OER cycle to form

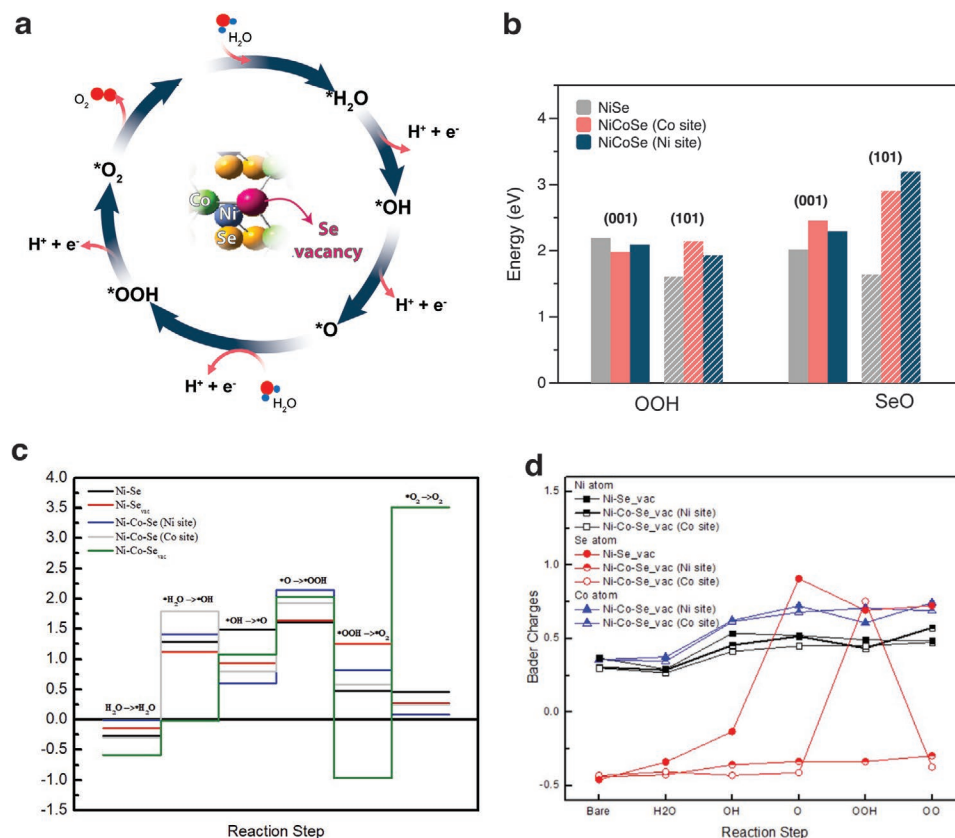


Figure 5. a) OER mechanism on the NiSe (101) surface, the Se vacancy is highlighted in magenta, Co doping sites are given in green, and Ni and Se are shown in blue and yellow, respectively. b) Comparing the energies of OOH formation and SeO desorption on (001) and (101) surfaces. c) The potential energy of reaction for Ni–Se, Ni–Se_{vac}, Ni–Co–Se, and Ni–Co–Se_{vac} (101) surfaces. d) Bader charge of Ni, Se, and Co atoms for Ni–Se, Ni–Se_{vac}, Ni–Co–Se, and Ni–Co–Se_{vac} (101) surfaces, respectively.

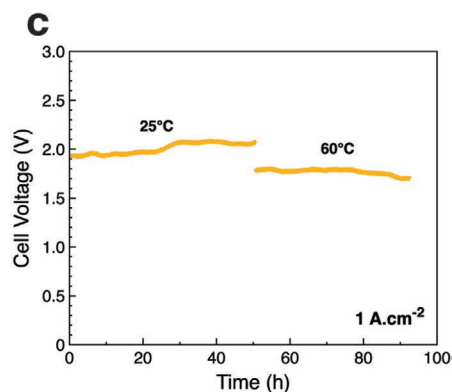
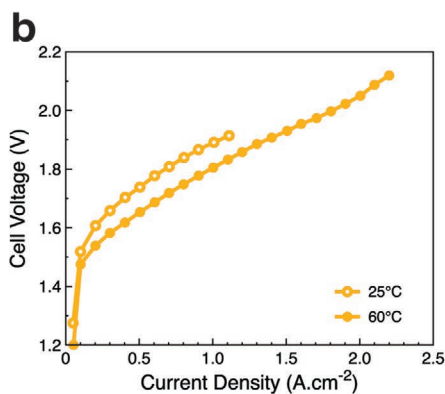
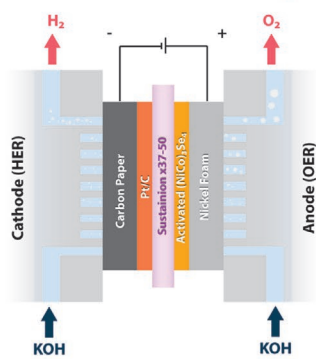
adsorbed peroxide on the surface. A comparison between the two processes is justified because the formation of adsorbed OOH on Ni–Se and Ni–Co–Se surfaces represents the potential rate determining step (Figure 5b). The enthalpies of both the OOH formation and SeO desorption were computed. As shown in Figure 5b, while both processes are enthalpically competitive on the Ni–Se surface, the SeO desorption is not enthalpically favored on the Ni–Co–Se surface. At a Ni site, the oxygen is also bonded to the nickel; therefore, SeO desorption would disrupt more surface interactions. At a Co site, the loss of a coordinating Se destabilizes the electron–hole created by the dopant, Co. Se leaching is not enthalpically favored over continuing the OER cycle, yet Se leaching has been observed experimentally, from which we propose that it is an entropically driven process.

The Ni–Se_{vac} and Ni–Co–Se_{vac} (101) surfaces were created by removing the Se atom that formed a bond with the adsorbed O atom on the Ni–Se and Ni–Co–Se (101) surfaces, respectively. OER intermediates were calculated again at the same adsorption sites to demonstrate the effects of a Se vacancy. The potential energy differences associated with the potential determining step do not decrease significantly with Co doping or a Se vacancy separately (Figure 5c and Figure S23, Supporting Information). These surface modifications have the same effect on the Ni–O distances for OER intermediates at a Ni site. The Ni–O distances for OH, O, OOH, and O₂ adsorbed on Ni–Se_{vac} and

Ni–Co–Se are between 1.9 and 2.1 Å which is much shorter than the Ni–O distances on Ni–Se, which were all above 3 Å. The Ni–O distances for H₂O on each (101) surface investigated were above 3 Å. The corresponding PDOS did not differ from those of the bare surfaces, and this indicates the water molecule does not interact strongly with the surface. Further discussion will be limited to the adsorbed OH, O, OOH, and O₂ species. Like the Ni–Co–Se (101) surface, the Ni–Se_{vac} (101) surface also shows a bond forming between another surface Se and the adsorbed oxygen atom. The Se–O interatomic distance is ≈1.8 Å, and the Bader charge shows the Se transfer of an electron to the adsorbed O atom on Ni–Se_{vac} (Figure 5d). This suggests the Se leaching may continue at a Ni site that has already lost a Se atom, although it will be less enthalpically favored than the first Se loss because both Ni–Se and Ni–O bonds will be disrupted.

The combination of Co-doping and a Se vacancy on the (101) surface behaves differently from the Ni–Se, Ni–Se_{vac}, and Ni–Co–Se surfaces discussed above. The potential determining step becomes the oxygen molecule desorption. The significantly higher O₂ desorption energy for the Ni–Co–Se_{vac} (101) surface is due to the second oxygen atom also binding to two metal atoms. The desorption from this surface breaks three Ni–O bonds and one Co–O bond, unlike Ni–Se, Ni–Se_{vac}, and Ni–Co–Se (101) surfaces where, at most, two metal–oxygen bonds are broken. The greater number of bonds between surface metal atoms and

a AEM Water Electrolyser



d CO2 Reduction

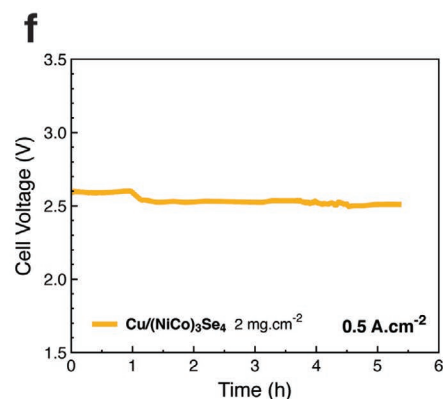
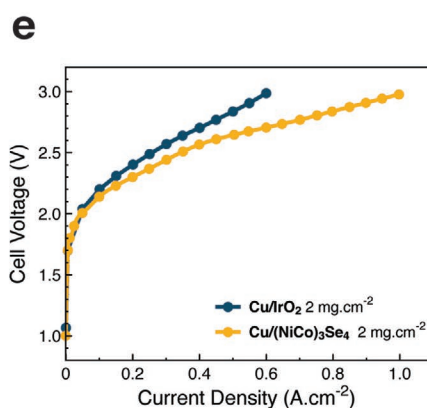
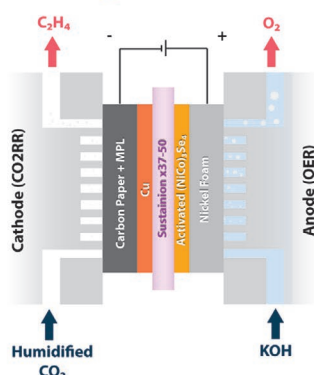


Figure 6. a) Schematic diagram of AEM water splitting. b) Polarization curve and c) chronopotentiometry test using $0.2 \text{ mg}_{\text{Pt}} \text{ cm}^{-2}$ Pt/C on carbon paper for HER and 2 mg cm^{-2} activated $(\text{NiCo})_3\text{Se}_4$ on nickel foam for OER. d) Schematic diagram of CO_2 reduction. e) Polarization curve and f) chronopotentiometry test using 1 mg cm^{-2} Cu on PTFE for CO_2R and 2 mg cm^{-2} activated $(\text{NiCo})_3\text{Se}_4$ on nickel foam for OER.

adsorbed oxygen atoms combined with the high O_2 desorption energy shows that, rather than lose O_2 through desorption, the $\text{Ni-Co-Se}_{\text{vac}}$ surface forms an active oxide layer.

In addition to the energetic differences, several structural and electronic features distinguish the $\text{Ni-Co-Se}_{\text{vac}}$ (101) surface from the Ni-Se , Ni-Co-Se , and $\text{Ni-Se}_{\text{vac}}$ surfaces. The metal–oxygen distances are shorter than those calculated on the Ni-Se , Ni-Co-Se , and $\text{Ni-Se}_{\text{vac}}$ surfaces. The Ni-O distances on $\text{Ni-Co-Se}_{\text{vac}}$ for OH, O, OOH, and O_2 are between 1.8 and 1.9 Å, while the Co-O distances are between 1.7 and 1.9 Å (Tables S7 and S9, Supporting Information). The distances for the Ni and Co sites on $\text{Ni-Co-Se}_{\text{vac}}$ are consistent with $\gamma\text{-NiOOH}$,^[37] and $\gamma\text{-CoOOH}$ ^[38] in agreement with the present EXAFS results and will cycle between these structures and their corresponding hydroxides throughout the OER.^[39,40] The distinction between a Ni and a Co site is lost on the $\text{Ni-Co-Se}_{\text{vac}}$ (101) surface due to the adsorbed oxygen species filling the Se vacancy and bridging a surface Co and Ni atom. The first adsorbed oxygen species replaces the desorbed Se atom to stabilize the electron hole created by the presence of Co. This simple substitution was not observed on $\text{Ni-Se}_{\text{vac}}$ and implied the original structure might be more preserved in $\text{Ni-Co-Se}_{\text{vac}}$ as the surface oxidation progresses. The ratio of the Ni Bader charges for the O, OOH, and O_2 intermediates on the Ni-Co-Se , $\text{Ni-Se}_{\text{vac}}$, and $\text{Ni-Co-Se}_{\text{vac}}$ surfaces compared with the Ni

Bader charge on the corresponding bare surfaces show the Ni has been oxidized from Ni^{+2} to Ni^{+3} . The $\text{Ni-Co-Se}_{\text{vac}}$ surface differs from the other two surfaces, as a similar analysis shows the Co atom is also oxidized to Co^{+3} . Furthermore, an electron transfer from a surface Se on $\text{Ni-Co-Se}_{\text{vac}}$ was only observed due to the secondary O atom in the OOH intermediate, otherwise, the Se Bader charges remained constant (Figure 5d). These electronic differences are confirmed through projected densities of states (Figure S27, Supporting Information) and agree with the present EELS results.

Our DFT calculations have shown that Se leaching is not an enthalpically favored process; so, it must be entropically driven. While the Ni-Co-Se , $\text{Ni-Se}_{\text{vac}}$, and $\text{Ni-Co-Se}_{\text{vac}}$ surface all showed the Ni atom becoming oxidized, the shortest metal–oxygen bonds and Co oxidation were only observed on the $\text{Ni-Co-Se}_{\text{vac}}$ surface. A surface Se atom only transferred an electron to the second oxygen atom adsorbed on the $\text{Ni-Co-Se}_{\text{vac}}$ surface contributing to the high energy of the O_2 desorption, thereby energetically favoring the surface restructuring to the active $\gamma\text{-NiCoOOH}$. The Bader charge analysis and calculated structures agree with the present experimental results. The resulting active surface is therefore NiCoOOH . The good OER activity observed experimentally is an agreement with a recent Shin et al.'s computational study^[13] which showed that $\gamma\text{-NiOOH}$ doped with Co had the lowest theoretical overpotential, 270 mV,

out of a range of transition metal dopants, including Fe.^[41,42] The study predicted that Co when doped with γ -NiOOH can help in the stabilization of the formation of O on the MO bond while the O–O coupling is catalyzed on Ni active sites, making the catalyst a much better OER catalyst than γ -NiOOH.

2.4. AEM Water and CO₂R Electrolyzer

To further evaluate the performance of activated (NiCo)₃Se₄ (NiCoOOH) as an OER electrocatalyst for industrial water splitting and CO₂R, we used a 5 cm² AEM electrolyzer with the cathodic reaction supported by Pt/C on carbon paper for hydrogen evolution and Cu on PTFE for CO₂R (Figure 6a,d). The polarization curves indicated that the catalyst lowered the cell voltage to 2 V at 2 A cm⁻² for water splitting (Figure 6b) and 3 V at 1 A cm⁻² for CO₂R using 1 M KOH, outperforming IrO₂ (Figure 6e). This performance was stable for 95 h at 1 A cm⁻² for water splitting (Figure 6c) and 5 h at 0.5 A cm⁻² for CO₂R (Figure 6f). These results demonstrated the potential of utilizing cryomilled (NiCo)₃Se₄ for industrial applications.

3. Conclusions

We have reported the synthesis of homogeneously dispersed Ni–Co–Se nanocrystals with varying compositions using solid-state cryomilling. Electrochemical leaching of Se from the structure facilitated the transformation to Ni/Co-oxyhydroxides as validated by DFT, TEM, sXAS, and in situ XAS. The best performing activated (NiCo)₃Se₄ electrocatalyst showed a stable OER performance drawing 0.5 A cm⁻² at 279 mV, and 1 A cm⁻² at 329 mV of overpotential for 500 h in 1 M Fe-free KOH. Integrating the electrocatalyst in an AEM electrolyzer, we could demonstrate an outstanding water splitting performance delivering 2 A cm⁻² at 2 V and CO₂R performance of 1 A cm⁻² at 3 V. The results encourage the utilization of cryomilling and chalcogenides, such as Se, to mass produce efficient earth-abundant electrocatalysts with long-term durability.

Supporting Information

Supporting Information is available from the Wiley Online Library or from the author.

Acknowledgements

This work was supported financially by the Natural Sciences and Engineering Research Council (NSERC) of Canada, Vanier Canada Graduate Scholarship, and TOTAL SE. Electron microscopy, scanning transmission electron microscopy, and electron energy loss spectroscopy were performed at the Canadian Centre for Electron Microscopy (CEEM) at McMaster University. This research used resources of the Advanced Photon Source, an Office of Science User Facility operated for the U.S. Department of Energy (DOE) Office of Science by Argonne National Laboratory and was supported by the U.S. DOE under Contract No. DE-AC02-06CH11357 and the Canadian Light Source and its funding partners. The authors thank Dr. Tianpin Wu and Dr. George Sterbinsky from 9BM beamline, and Dr. Debora Motta Meira and Dr. Zou Finrock

from 20BM beamline for assistance in collecting the XAS data and at the advanced photo source (APS). DFT calculations were conducted as part of the Engineered Nickel Catalysts for Electrochemical Clean Energy project administered from Queen's University and supported by Grant No. RGPNM 477963-2015 under the Natural Sciences and Engineering Research Council of Canada (NSERC) Discovery Frontiers Program. The computational resources were provided by Compute Canada.

Conflict of Interest

The authors declare no conflict of interest.

Data Availability Statement

Research data are not shared.

Keywords

CO₂ reduction, cryomilling, oxygen evolution reaction, PGM-free X-ray absorption spectroscopy

Received: May 19, 2021

Revised: August 4, 2021

Published online:

- [1] P. P. Sharma, X. D. Zhou, *Wiley Interdiscip. Rev. Energy Environ.* **2017**, 6, e239.
- [2] P. De Luna, C. Hahn, D. Higgins, S. A. Jaffer, T. F. Jaramillo, E. H. Sargent, *Science* **2019**, 364, eaav3506.
- [3] C.-T. Dinh, G. Kibria, A. Seifitokaldani, A. Kiani, O. S. Bushuyev, C. Zou, R. Quintero-Bermudez, E. H. Sargent, T. Burdyny, C. M. Gabardo, J. P. Edwards, Y. Pang, D. Sinton, P. DeLuna, *Science* **2018**, 360, 783.
- [4] J. R. Galán-Mascarós, *ChemElectroChem* **2015**, 2, 37.
- [5] H. Zhou, F. Yu, Q. Zhu, J. Sun, F. Qin, L. Yu, J. Bao, Y. Yu, S. Chen, Z. Ren, *Energy Environ. Sci.* **2018**, 11, 2858.
- [6] M. Yu, G. Moon, E. Bill, H. Tüysüz, *ACS Appl. Energy Mater.* **2019**, 2, 1199.
- [7] M. Gong, Y. Li, H. Wang, Y. Liang, J. Z. Wu, J. Zhou, J. Wang, T. Regier, F. Wei, H. Dai, *J. Am. Chem. Soc.* **2013**, 135, 8452.
- [8] C. Liang, P. Zou, A. Nairan, Y. Zhang, J. Liu, K. Liu, S. Hu, F. Kang, H. J. Fan, C. Yang, *Energy Environ. Sci.* **2019**, 13, 86.
- [9] C. Kuai, Z. Xu, C. Xi, A. Hu, Z. Yang, Y. Zhang, C. Sun, L. Li, D. Sokaras, C. Dong, S. Qiao, X. Du, F. Lin, *Nat. Catal.* **2020**, 3, 743.
- [10] F. D. Speck, K. E. Dettelbach, R. S. Sherbo, D. A. Salvatore, A. Huang, C. P. Berlinguette, *Chem* **2017**, 2, 590.
- [11] D. Y. Chung, P. P. Lopes, P. Farinazzo Bergamo Dias Martins, H. He, T. Kawaguchi, P. Zapol, H. You, D. Tripkovic, D. Strmcnik, Y. Zhu, S. Seifert, S. Lee, V. R. Stamenkovic, N. M. Markovic, *Nat. Energy* **2020**, 5, 222.
- [12] M. Wang, Z. Dang, M. Prato, D. V. Shinde, L. De Trizio, L. Manna, *ACS Appl. Nano Mater.* **2018**, 1, 5753.
- [13] H. Shin, H. Xiao, W. A. Goddard, *J. Am. Chem. Soc.* **2018**, 140, 6745.
- [14] X. Fu, D. N. Beatty, G. G. Gaustad, G. Ceder, R. Roth, R. E. Kirchain, M. Bustamante, C. Babbitt, E. A. Olivetti, *Environ. Sci. Technol.* **2020**, 54, 2985.
- [15] W. Li, D. Xiong, X. Gao, L. Liu, *Chem. Commun.* **2019**, 55, 8744.
- [16] W. Li, X. Gao, D. Xiong, F. Wei, W. G. Song, J. Xu, L. Liu, *Adv. Energy Mater.* **2017**, 7, 1602579.

- [17] R. Gao, G. D. Li, J. Hu, Y. Wu, X. Lian, D. Wang, X. Zou, *Catal. Sci. Technol.* **2016**, *6*, 8268.
- [18] M. Cui, C. Yang, B. Li, Q. Dong, M. Wu, S. Hwang, H. Xie, X. Wang, G. Wang, L. Hu, *Adv. Energy Mater.* **2021**, *11*, 2002887.
- [19] L. Schultz, *Mater. Sci. Eng.* **1988**, *97*, 15.
- [20] W. L. Johnson, *Prog. Mater. Sci.* **1986**, *30*, 81.
- [21] K. B. Dhanalakshmi, S. Latha, S. Anandan, P. Maruthamuthu, *Int. J. Hydrogen Energy* **2001**, *26*, 669.
- [22] K. Fan, H. Zou, Y. Lu, H. Chen, F. Li, J. Liu, L. Sun, L. Tong, M. F. Toney, M. Sui, J. Yu, *ACS Nano* **2018**, *12*, 12369.
- [23] C. Suryanarayana, *Mechanical Alloying and Milling*, CRC Press, Boca Raton, FL, USA **2004**.
- [24] D. Zheng, M. Li, Y. Li, C. Qin, Y. Wang, Z. Wang, *Beilstein J. Nanotechnol.* **2019**, *9*, 281.
- [25] W. Shi, F. Guo, C. Zhu, H. Wang, H. Li, H. Huang, Y. Liu, Z. Kang, *J. Mater. Chem. A* **2017**, *5*, 19800.
- [26] B. Akabayov, C. J. Doonan, I. J. Pickering, G. N. George, I. Sagi, *J. Synchrotron Radiat.* **2005**, *12*, 392.
- [27] Y. Liang, Y. Li, H. Wang, J. Zhou, J. Wang, T. Regier, H. Dai, *Nat. Mater.* **2011**, *10*, 780.
- [28] D. Meyers, S. Mukherjee, J. G. Cheng, S. Middey, J. S. Zhou, J. B. Goodenough, B. A. Gray, J. W. Freeland, T. Saha-Dasgupta, J. Chakhalian, *Sci. Rep.* **2013**, *3*, 1834.
- [29] M. Al Samarai, A. W. Hahn, A. Beheshti Askari, Y. T. Cui, K. Yamazoe, J. Miyawaki, Y. Harada, O. Rüdiger, S. Debeer, *ACS Appl. Mater. Interfaces* **2019**, *11*, 38595.
- [30] C. Xiao, X. Lu, C. Zhao, *Chem. Commun.* **2014**, *50*, 10122.
- [31] H. A. El-Sayed, A. Weiß, L. F. Olbrich, G. P. Putro, H. A. Gasteiger, *J. Electrochem. Soc.* **2019**, *166*, F458.
- [32] B. G. Amin, A. T. Swesi, J. Masud, M. Nath, *Chem. Commun.* **2017**, *53*, 5412.
- [33] P. F. Wang, Y. J. Guo, H. Duan, T. T. Zuo, E. Hu, K. Attenkofer, H. Li, X. S. Zhao, Y. X. Yin, X. Yu, Y. G. Guo, *ACS Energy Lett.* **2017**, *2*, 2715.
- [34] B. Das, M. V Reddy, B. V. R. Chowdari, *Nanoscale* **2013**, *5*, 1961.
- [35] S. R. Mellsop, A. Gardiner, B. Johannessen, A. T. Marshall, *Electrochim. Acta* **2015**, *168*, 356.
- [36] H.-Y. Wang, Y.-Y. Hsu, R. Chen, T.-S. Chan, H. M. Chen, B. Liu, *Adv. Energy Mater.* **2015**, *5*, 1500091.
- [37] D. Friebe, M. W. Louie, M. Bajdich, K. E. Sanwald, Y. Cai, M. Wise, M. Cheng, D. Sokaras, T. Weng, R. Alonso-Mori, R. C. Davis, J. R. Bargar, J. K. Nørskov, A. Nilsson, A. T. Bell, *J. Am. Chem. Soc.* **2015**, *137*, 1305.
- [38] J. Huang, J. Chen, T. Yao, J. He, S. Jiang, Z. Sun, Q. Liu, W. Cheng, F. Hu, Y. Jiang, Z. Pan, S. Wei, *Angew. Chem., Int. Ed.* **2015**, *54*, 8722.
- [39] C. Marini, B. Joseph, S. Caramazza, F. Capitani, M. Bendele, I. Kantor, P. Lotti, O. Mathon, S. Pascarelli, P. Postorino, *High Pressure Res.* **2017**, *37*, 1.
- [40] D. Totir, Y. Mo, S. Kim, M. R. Antonio, D. A. Scherson, *J. Electrochem. Soc.* **2000**, *147*, 4594.
- [41] J. Zaffran, M. C. Toroker, *ChemistrySelect* **2016**, *1*, 911.
- [42] F. Costanzo, *Phys. Chem. Chem. Phys.* **2016**, *18*, 7490.